

Hybrid Self-Assembling Peptide/Gelatin Methacrylate (GelMA) Bioink Blend for Improved Bioprintability and Primary Myoblast Response

Mitchell Boyd-Moss, Kate Firipis, Anita Quigley, Aaqil Rifai, Artur Cichocki, Sarah Whitty, Catherine Ngan, Chaitali Dekiwadia, Benjamin Long, David R. Nisbet, Robert Kapsa, and Richard J. Williams*


Organ fabrication as the solution to renewable donor demands requires the ability to spatially deposit viable cells into biologically relevant constructs; necessitating reliable and effective cell deposition through bioprinting and the subsequent ability to mature. However, effective bioink development demands advances in both printability and control of cellular response. Effective bioinks are designed to retain shape fidelity, influence cellular behavior, having bioactive morphologies stiffness and highly hydrated environment. Hybrid hydrogels are promising candidates as they reduce the need to re-engineer materials for tissue-specific properties, with each component offering beneficial properties. Herein, a multicomponent bioink is developed whereby gelatin methacrylate (GelMA) and fluorenylmethoxycarbonyl-protected self-assembling peptides (Fmoc-SAPs) undergo coassembly to yield a tuneable bioink. This study shows that the reported fibronectin-inspired fmoc-SAPs present cell attachment epitopes RGD and PHSRN in the form of bioactive nanofibers; and that the GelMA enables superior printability, stability in media, and controlled mechanical properties. Importantly, when in the hybrid format, no disruption to either the methacrylate crosslinking of GelMA, or self-assembled peptide fibril formation is observed. Finally, studies with primary myoblasts show over 98% viability at 72 h and differentiation into fused myotubes at one and two weeks demonstrate the utility of the material as a functional bioink for muscle engineering.

1. Introduction

Recent advances in tissue engineering have provided significant promise to patients suffering severe tissue or organ loss because of disease or trauma. Advances in additive manufacturing, material science, and cell biology have led to the development of bioprinting, enabling the spatiotemporal control of signals, proteins, and cells within a single construct.^[1] Bioprinting provides the fabrication of custom, highly engineered artificial tissue scaffolds with precise control over micro- and macro-architecture.^[2,3] Furthermore, bioprinting allows for multimaterial printing enabling gradient presentation of biologically relevant signaling motifs.^[4] Despite the significant advance in bioprinting technique development, current approaches are still significantly limited by the availability of effective bioinks; with many bioinks unable to simultaneously satisfy biological and mechanical requirements demanded by bioprinting practices.^[5]

Gelatin methacrylate (GelMA) is a commonly used biomaterial for soft-tissue

M. Boyd-Moss, K. Firipis, A. Quigley, A. Cichocki, S. Whitty, C. Ngan, D. R. Nisbet, R. Kapsa, R. J. Williams
BioFab3D
Aikenhead Centre for Medical Discovery
St Vincent's Hospital Melbourne
Fitzroy 3065, Australia
E-mail: Richard.Williams@deakin.edu.au

 The ORCID identification number(s) for the author(s) of this article can be found under <https://doi.org/10.1002/anbr.202100106>.

© 2021 The Authors. Advanced NanoBiomed Research published by Wiley-VCH GmbH. This is an open access article under the terms of the Creative Commons Attribution License, which permits use, distribution and reproduction in any medium, provided the original work is properly cited.

DOI: 10.1002/anbr.202100106

M. Boyd-Moss, K. Firipis, A. Quigley, A. Cichocki, S. Whitty, R. Kapsa
School of Engineering
RMIT University
Melbourne, VIC 3000, Australia

M. Boyd-Moss, A. Rifai, R. J. Williams
IMPACT
School of Medicine
Deakin University
Waurin Ponds, VIC 3216, Australia

C. Dekiwadia
RMIT Microscopy and MicroAnalysis Facility
RMIT University
Melbourne, VIC 3000, Australia

bioprinting applications.^[6,7] Bioinks developed from GelMA possess highly favorable mechanical properties, boasting thermo-reversible gelation, high biocompatibility, biodegradability, bioactivity, and, importantly, the ability to undergo irreversible photocrosslinking.^[8] However, GelMA is limited in the ability to target multiple tissue types via modification of bioactive motif presentation;^[9] therefore, further functionalization may be beneficial. GelMA is additionally limited in its morphology, with recent attempts to form fibril-like structures from electrospinning.^[10] Degree of functionalization (DoF) is an important consideration to take into account when using GelMA hydrogels. Our previous study investigated the influence of DoF on material mechanics and architecture, finding that low methacrylate GelMA (LM-GelMA, 18% DoF) exhibits beneficial nanostructure, gelation temperature, and strain tolerance over higher methacrylations.^[11] Interest is growing in LM-GelMA for soft tissue engineering. The low degree of methacrylate of LM-GelMA permits the maintenance of a soft gel, ideal for soft tissues due to cellular mechanotransduction.^[12,13] However, attempts to translate LM-GelMA to bioink development have returned disappointing, with LM-GelMA unable to maintain shape fidelity.^[14]

Self-assembling peptides (SAPs) are a unique class of low-molecular-weight peptides that spontaneously immobilize their surrounding fluid to form large, biologically relevant structures.^[15] The ability of SAPs to be synthesized using routine peptide synthesis practices allows for significant control over structural and biochemical properties; enabling targeted cell signaling via incorporation of specific cell signaling motifs in the form of amino acid sequences.^[16] Aromatically capped peptide derivatives, including Fmoc-SAPs, have seen substantial success in muscle^[15,17] and neural regenerative applications,^[18,19] and are growing in interest as bioinks.^[20]

Fmoc-FRGDF is a fibronectin-inspired SAP which has demonstrated success both *in vitro*^[17] and *in vivo*.^[18] Fmoc-FRGDF forms fibrous structures that are highly reminiscent of the native extracellular matrix (ECM) via a well-characterized pH switch method, resulting in the development of a highly hydrated hydrogel.^[21] Similarly, Fmoc-PHSRN is a fibronectin-inspired SAP presenting RGD-synergistic cell-attachment motif, "PHSRN." Previous work in our laboratory has focused on the coassembly of these peptides within a single construct. The combination of these two peptide sequences during assembly has been shown to enhance human mammary fibroblast cell attachment, spreading and proliferation *in vitro*.^[22] Further functionalization and tuning of Fmoc-FRGDF has also been achieved via hybrid assembly with developmentally and structurally important macromolecules, including agarose,^[23] versican, and fucoidan.^[24–26] The ability of Fmoc-FRGDF to associate with macromolecules

enables the novel development of hybrid scaffolds, increasing the versatility of these materials. However, despite success in regenerative capacities, these self-assembling materials have been limited in use as bioinks by a lack of rapid gelation after high shear forces experienced during extrusion. To our knowledge, no previous work has been carried out on the development of bioactive motif presenting Fmoc-SAP-blends as photocrosslinkable bioinks.

In this work, we take advantage of the high mechanical tunability of GelMA and the bioactive tunability of Fmoc-SAPs, to prototype the development of hybrid bioinks with high bioactivity and printability. We investigate the association between Fmoc-FRGDF/PHSRN and LM-GelMA and determine the mechanisms driving self-assembly and gelation. Subsequently, we investigate the network topology, stiffness, and printability, before finally investigating biocompatibility using primary myoblasts. The principal goal of this study is to investigate the potential use of such hybrid systems as bioink toolkits, enabling ease of customization through alteration of SAP sequence; and providing the foundation for further bioink development custom to alternate tissue types. Our findings change the paradigm that hybrid Fmoc-SAPs cannot be used as effective bioinks and demonstrate that bioprintability outcomes of high shape fidelity and cellular support can occur using hybrid LM-GelMA/SAP bioinks.

2. Results

2.1. Formation of Bioinks

We have previously demonstrated the synergistic behavior of hydrogels formed from fibronectin-inspired Fmoc-FRGDF and Fmoc-PHSRN.^[22] In this study, we advance this hydrogel system into an effective bioink by the inclusion of LM-GelMA. Three hybrid bioinks were developed. First, a fibronectin-inspired Fmoc-SAP containing synergistic fibronectin attachment motifs, RGD and PHSRN, was self-assembled under physiological conditions (pH 7.4) using a well-characterized pH switch method.^[27] Here, Fmoc-FRGDF and Fmoc-PHSRN were coassembled in accordance with our previous study (**Figure 1**), from here termed coassembled.^[22] A second bioink was developed through the low degree (34%) methacrylation of gelatin to form LM-GelMA, which was dissolved in PBS such that the final concentration was 6% w/v (Figure 1). This LM-GelMA formulation (34% DoF, 6% w/v) has been selected owing to its enhanced gelation temperature and predicted suitability for bioink integration.^[11] LM-GelMA can undergo photocrosslinking when subjected to UV irradiation in the presence of a photoinitiator, allowing for controlled and rapid gelation. A third bioink was assembled

B. Long
Faculty of Science and Technology
Federation University
Mt. Helen, VIC 3350, Australia

D. R. Nisbet
The Graeme Clark Institute
The University of Melbourne
Melbourne 3000, Australia

D. R. Nisbet
Department of Biomedical Engineering
Faculty of Engineering and Information Technology
The University of Melbourne
Melbourne 3000, Australia

D. R. Nisbet
Research School of Engineering
Australian National University
Canberra, ACT 0200, Australia

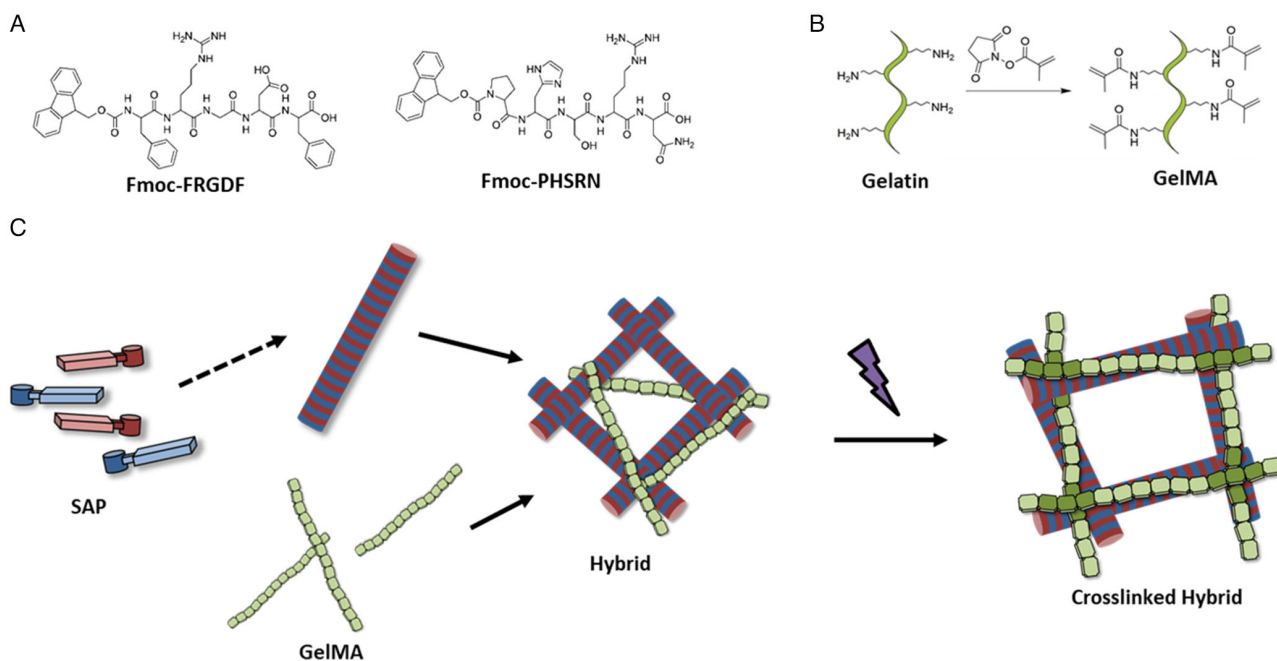


Figure 1. A) Chemical structure of Fmoc-FRGDF and Fmoc-PHSRN. B) Schematic detailing gelatin modification with methacrylate groups to produce gelatin methacrylate. C) Schematic representation of assembly mechanisms showing self-assembly of Fmoc-SAPs into fibrils in the presence of gelatin methacrylate before subsequent photocrosslinking of the network.

through a combination of Fmoc-FRGDF/Fmoc-PHSRN hydrogel with LM-GelMA hydrogel (Figure 1). Hereafter, this gel is termed FPG-Hybrid. Both the coassembled bioink and the FPG-hybrid bioink were observed to present self-supporting gel-like morphologies at 20 °C, remaining stable even once inverted (Figure S1, Supporting Information). Contrastingly, LM-GelMA did not demonstrate noticeable gel-like properties at this temperature and subsequently was found to flow to the bottom upon tube inversion. All bioinks were observed to be clear upon assembly.

2.2. Visualization of Assembled Structures and Network Architecture

Underlying structural and network morphologies of the developed bioinks were visualized using transmission electron microscopy (TEM), cryo-scanning electron microscopy (CryoSEM) and Small-Angle-Xray-Scattering (SAXS) (Figure 2).

2.2.1. Transmission Electron Microscopy

Transmission Electron Microscopy (TEM) provided insight into the nanoscale structures present in each bioinks (Figure 2D–F). The coassembled bioink was observed to possess fibrillar structures as is characteristic with this type of assembly.^[22] These fibrillar structures were not evident in LM-GelMA samples, rather aggregates were observed. The hybrid bioink containing both Fmoc-FRGDF/Fmoc-PHSRN and LM-GelMA demonstrated fibrillar structures comparable to those seen in the coassembled sample alone. Fibril diameter was quantified using Image-J analysis for coassembled and hybrid samples.

An average fibril diameter of 15.06 nm ($\sigma = 0.22$ nm) was observed for coassembled samples while the hybrid sample was shown to have slightly smaller fibrils of 13.12 nm ($\sigma = 1.00$). Despite a slight decrease in fibril diameter in hybrid samples, both were shown to maintain fibril formation.

2.2.2. Cryo Scanning Electron Microscopy (CryoSEM)

Investigation into network microstructure was observed through CryoSEM, allowing for sample network topology to be visualized in its native, hydrated state with minimal compromise to structure.^[28] Briefly, samples were plunge-frozen through liquid nitrogen to form amorphous ice before being fractured and sublimated. In each sample, network morphology was analyzed before and after subsection to UV irradiation (Figure 2G–L). Representative images were acquired for each sample and a comparison was made between hydrogel microstructures. The coassembled bioink demonstrated a chaotic fibrillar architecture both before and after UV subsection with no significant change in structure (Figure 2G, J). Contrastingly, LM-GelMA was observed to present as a jagged network before UV subsection (Figure 2H) and transitioned into a more ordered topology with a honeycomb-like structure following UV exposure (Figure 2K). Interestingly, the FPG-hybrid sample appeared to contain both network morphologies before UV crosslinking, with nanofibrils and jagged, LM-GelMA-like, networks both evident (Figure 2I). However, after UV exposure, the network was found to become more ordered, following a similar trend to the crosslinked LM-GelMA sample (Figure 2L). These results suggest that the FPG-hybrid sample possesses fibrillar structures owing to the presence of the SAP network, and structural aspects relating

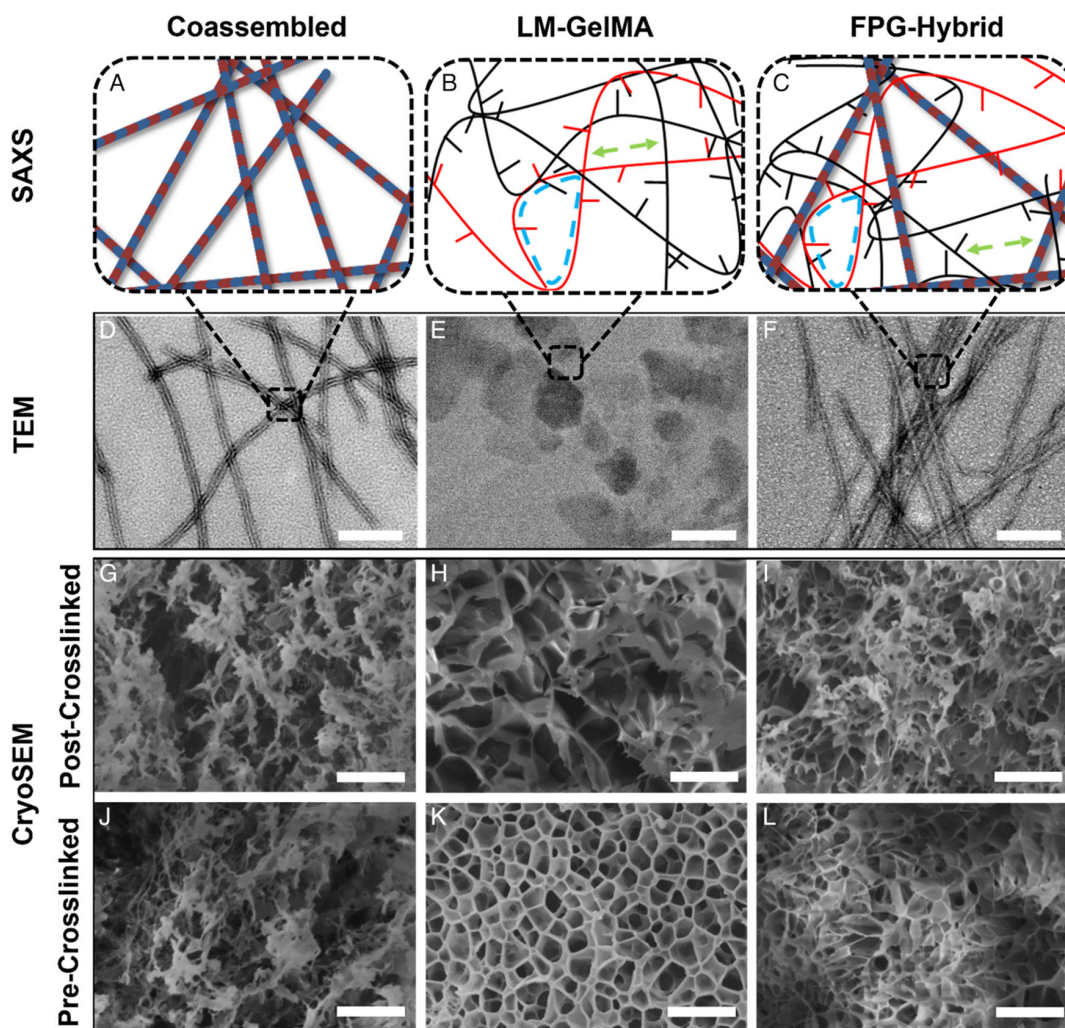


Figure 2. A–C) Schematic representation of proposed nanostructure as determined by SAXS. Showing SAXS characteristics B,C), fractal dimension (Red) correlation length (Green), mesh size (Blue). D–F) TEM analysis of material nanostructure (Scale Bar: 200 nm) (Arrows point to fibrous structure), G–I) CryoSEM analysis of network microstructure prior to UV exposure, and J–L) CryoSEM analysis of network microstructure following UV exposure. From left to right: Coassembled Fmoc-FRGDF/Fmoc-PHSRN, LM-GelMA, and FPG-hybrid samples. (Scale Bars: 100 μm).

to LM-GelMA addition. Importantly, the presence of LM-GelMA during self-assembly did not appear to influence fibril formation in the FPG-hybrid. Furthermore, a significant structural change was evident in LM-GelMA containing samples upon subjection to UV irradiation, as generally observed in photocrosslinkable samples.

2.3. Investigation of Assembled Structures and Mechanical Properties

2.3.1. Small Angle X-Ray Scattering (SAXS)

SAXS is a powerful tool that allows the probing of nanoscale configurations within polymer systems providing insights into material features such as nanostructure size and shape. SAXS has the benefit over TEM and CryoSEM in that it measures the sample without the need for sample preparation steps such as dilution,

freezing, and staining. SAXS scattering curves were collected (Figure 3A) and analyzed (Figure 3B and S2, Supporting Information) to determine the average fiber radius, which could be directly compared with TEM measures of fiber width and provide insights into the nanoscale network branching and length between structures and whether these were altered in the presence of GelMA. Coassembled Fmoc-FRGDF/Fmoc-PHSRN has previously been shown to form cylindrical structures, such as fibers, as indicated through q^{-4} shifting to a q^{-1} dependence at low q range and a comparable trend was observed in this instance.^[22] Despite indications of fibrillar structures in FPG-hybrid TEM analysis, both LM-GelMA containing samples did not sufficiently satisfy a cylindrical model and therefore were fitted using shape independent models. Recent research within our laboratory using SAXS has revealed the nanostructural changes of GelMA, including LM-GelMA, in response to DoF, macromer concentration, and UV crosslinking.^[11]

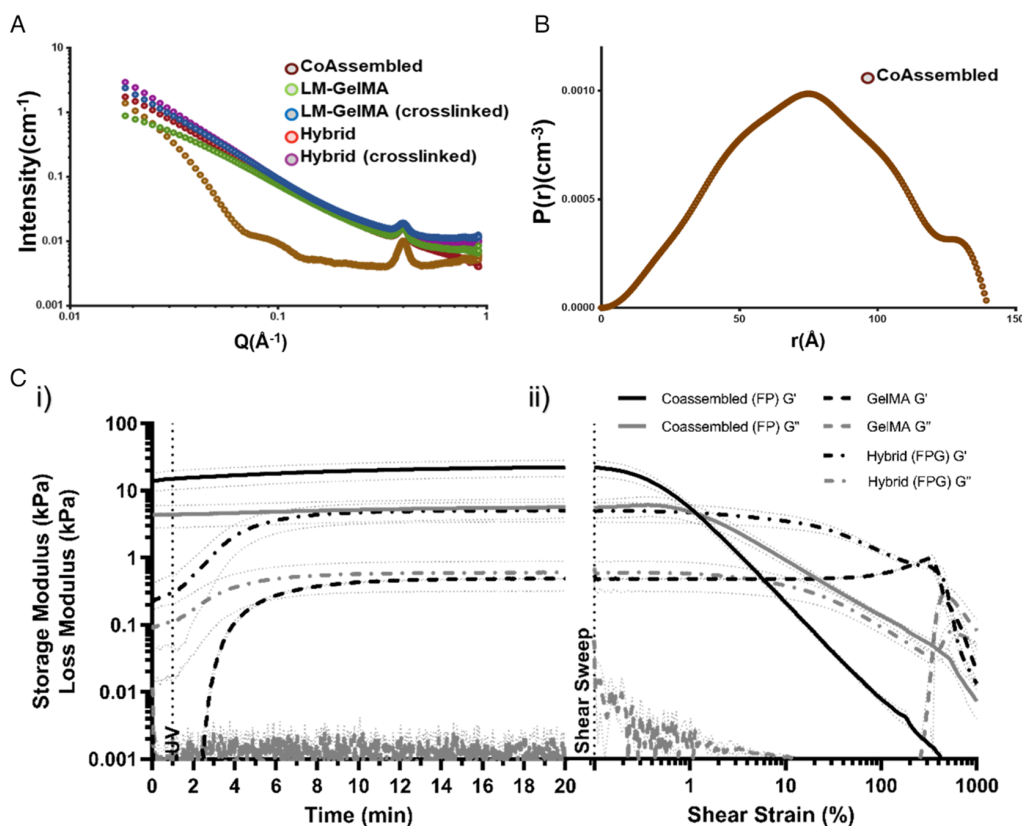


Figure 3. A) SAXS curves of Fmoc-FRGDF/Fmoc-PHSRN, LM-GelMA, and FPG-hybrid samples. B) Resultant probability of average fibril radius modelled using $P(r)$ function (SASView) of coassembled. C) Rheological analysis of i) in situ crosslinking and ii) post-crosslinking material resistance to shear strain, where dashed line at 1 min indicates where UV was turned on and dashed line after 20 min indicates where shear sweep begins. G' storage modulus (black lines) G'' loss modulus (dark grey lines) represented as the mean of triplicate tests, light grey lines indicate \pm STD.

A schematical representation of SAXS characteristics is shown in Figure 2A–C.

SAXS—Calculation of Average Fibril Diameter: Indirect Fourier transform (IFT) analysis was performed on the coassembled sample to calculate average fibril radius via application of the $P(r)$ function (SASview) (Figure 3B and S2D, Supporting Information). TEM analysis indicated fibril length lies outside of the q -range, and therefore, the value resulting in the maximum $P(r)$ intensity was attributed to fibril radius. Analysis of $P(r)$ fitting indicated average fibril diameter of 15.0 nm ($r = 75.2 \text{ \AA}$) for the 5 mg mL^{-1} coassembled sample. Analysis of average fibril diameter was in agreement with previous studies^[22] and observations made during TEM analysis.

SAXS – Determination of Mass-Fractal Dimension: Considering LM-GelMA containing samples did not sufficiently satisfy a cylinder model, shape independent analysis was performed on both pre- and post-crosslinked samples. Analysis of scattering power or “mass-fractal dimension” was calculated for each LM-GelMA containing sample before and after crosslinking (Figure S2A, Supporting Information). The linear region of scattering plots on a log–log scale was used to calculate mass-fractal dimension, d_m , which quantifies self-similar organizations over a range of length scales, and consequently offered insight into polymer structure and conformation.^[29] The mass-fractal dimension ranges from 1 to 3; a mass-fractal dimension of 1 indicates a

linear, 1D object, while a mass-fractal dimension near 1.67 is associated with swollen polymer coils in a good solvent. Mass-fractal dimensions exceeding 2 indicate branched polymer configurations and are typical of chemically crosslinked systems.^[30,31] The mass-fractal dimension can be described by Equation (1), wherein A is a scaling factor.

$$I(q) = \frac{A}{q^{d_m}} \quad (1)$$

Analysis of mass-fractal dimension for each LM-GelMA containing sample across mid- q -range ($0.05\text{--}0.2 \text{ nm}^{-1}$) revealed a relatively low value for pre-crosslinked LM-GelMA of 1.797 ± 0.006 . Upon subjection to UV irradiation, the mass-fractal dimension is found to increase to 2.123 ± 0.005 , as is expected with covalently crosslinked systems. In comparison, the FPG-hybrid sample demonstrated an initial mass-fractal dimension of 2.089 ± 0.005 before crosslinking, and this increased to 2.253 ± 0.005 following UV exposure. These results indicated that all systems demonstrate an increase in polymer conformation complexity toward branched systems as is characteristic of similar gelatin-based crosslinking systems.^[11,31] Importantly, polymers in the FPG-hybrid system were initially branched to a greater degree, and upon UV subjection, retain their ability to crosslink further through the formation of

covalent bonds, resulting in polymer conformations of greater complexity, likely due to the presence of nanostructured SAP fibrils.

SAXS—Determination of Correlation Length: The correlation length of LM-GelMA and FPG-hybrid samples was determined across the mid-low q -range (Figure S2B, Supporting Information) using the correlation length model as described in Equation (2).

$$I(q) = \left(\frac{C}{(1 + Q\xi)^m} \right) + bkg \quad (2)$$

C is the Porod scaling factor which relates to the scattering intensity extrapolated to the scattering vector $q = 0$. bkg takes background scattering into account while the Porod exponent (m) provides information relating to the local polymer structure. ξ represents the correlation length and provides a reasonable estimate of average entanglement length for semi-dilute polymer solutions.^[30] Pre-crosslinked LM-GelMA demonstrates the lowest correlation length of all samples, exhibiting a correlation length (ξ) of 4.07 nm (± 0.03 nm). Upon photocrosslinking of LM-GelMA, the correlation length was found to increase to 5.91 nm (± 0.06 nm). The FPG-hybrid sample demonstrated an initial correlation length of 8.31 nm (± 0.16 nm) before crosslinking, and shifted to 7.52 nm (± 0.14 nm) in post-crosslinked samples; interestingly, this trend appears to be in agreement with similar gelatin-based crosslinking investigations, wherein correlation length was found to decrease upon crosslinking.^[31] This is likely due to increased network densification upon crosslinking, resulting in the formation of new junctions and subsequently, a decrease in correlation length.^[32] A possible explanation for the alternate trend experienced by LM-GelMA alone can be provided by Lindemann et al. wherein it was reported that more reactive crosslinkers resulted in an increase in correlation length.^[33] Despite both samples in this study using the same crosslinker and crosslinking concentration, GelMA experienced a greater change in mass-fractal dimension, and subsequently, demonstrated a greater structural change over the same crosslinking time.

The Porod exponent, m , provides insight into polymer conformational changes in a similar way to the mass-fractal dimension. Here, the Porod Exponent ranged from 2.04 to 2.28, comparable with similar assemblies.^[31] Once again, Porod exponent was found to increase with covalent crosslinking, reinforcing observations made through mass-fractal dimension calculation (Table S1, Supporting Information).

SAXS—Determination of Mesh Size: Determination of mesh size provides insight into interpolymer relations. Mesh size can be estimated by finding the point of crossover (q_c) when scattering profiles are fit with a two-power law model. This point can also be described as the position of a shoulder formed at low scattering vectors, relating to structures of comparable dimensions.^[31] The determination of mesh size at this vector can be described by Equation (3).

$$\text{Mesh Size} = \frac{2\pi}{q_c} \quad (3)$$

Analysis of mesh size demonstrated a decrease upon crosslinking, from 13.64 nm (± 0.17 nm) to 10.74 nm (± 0.06 nm)

in LM-GelMA samples, and from 10.34 nm (± 0.10 nm) to 9.05 nm (± 0.11 nm) in FPG-hybrid samples (Figure S2C, Supporting Information). These results are in agreement with mass fractal dimension calculations and similar gelatin-based assemblies; wherein an increase in mass fractal dimension resulted in increased network formation and densification through the formation of covalent crosslinks.^[11,31] Consequently, this densification reduces the distance between polymers and results in reduced mesh size upon crosslinking.^[31] The reduced mesh-size between FPG-Hybrid samples and GelMA samples is likely due to the addition of the coassembled Fmoc-SAP nanofibers, which may increase crosslink number density between GelMA macromers, as is anticipated in similar, gelatin-nanocomposite systems.^[34] Assembly mechanisms were further confirmed through circular dichroism, FT-IR, and fluorescence spectroscopy. Data demonstrated maintenance of π - β assemblies in coassembled and FPG-hybrid samples as are characteristic of Fmoc-systems however spectra were heavily influenced by GelMA interactions (Figure S3, Supporting Information).

2.3.2. Mechanical Characteristics

Rheology—in Situ Crosslinking: Oscillatory rheology was used to determine mechanical changes during in situ photocrosslinking (Figure 3Ci). The UV source (356 nm, 4.5 mW cm⁻¹) was turned on 1 min after test commencement. As expected, the coassembled hydrogel demonstrated no significant change in modulus throughout UV exposure, exhibiting a storage modulus (G') of ≈ 20 kPa. Contrastingly, a notable change in storage modulus was observed in both the FPG-hybrid sample and in LM-GelMA alone, increasing significantly upon UV subjection. LM-GelMA demonstrated an initial G' of ≈ 0.1 Pa and this increased to 485 kPa. Similarly, the FPG-hybrid sample increased substantially upon UV exposure, from G' 220 to 5000 Pa. Typical hydrogels demonstrate a storage modulus of greater magnitude than their corresponding loss modulus (G''); as such, both SAP-containing samples were found to present as stable hydrogels before UV subjection in accordance with macroscopic observations (Figure S1, Supporting Information). After UV subjection, all three samples were found to demonstrate typical hydrogel viscoelastic properties with G' greater than G'' .

In this study, crosslinking completion was defined as the point where G' rate of change fell below 0.1% s⁻¹, indicating a plateau in crosslinking (Figure S5, Supporting Information). LM-GelMA required the longest time to reach crosslinking completion, requiring ≈ 8.4 min of UV subjection (9.4 min of testing). Alternatively, the FPG-hybrid material required only 7 min of UV exposure (8 min of the test) to reach a similar rate. A possible explanation for LM-GelMA hydrogels requiring more crosslinking time to reach a similar rate may be attributed to the requirement for greater polymer conformation change, as indicated through SAXs mass fractal dimension calculations. A further contributing factor could be the magnitude of change each sample experiences, with LM-GelMA samples experiencing a change of approximately three orders of magnitude compared to the FPG-hybrid hydrogel, which only experienced a change of one order of magnitude. For all subsequent tests, both samples

were subject to UV crosslinking for 500 s (8.3 min) to maintain consistency.

Rheology—Effect of Shear Strain: A notable factor limiting the use of these Fmoc-SAPs in bioprinting to date is their propensity to swell in media. Fmoc-SAPs' propensity to swell coupled with their inability to undergo rapid gelation after shear thinning, resulting in poor shape fidelity, has rendered these peptides ineffective for bioink development to date (Figure S5, Supporting Information). Therefore, SAP-incorporating bioinks which can withstand increased shear-strain post printing would be of substantial benefit to bioprinting applications.

Oscillatory rheology was employed to investigate hydrogel response to shear-strain following UV exposure for all samples. Samples were subjected to an amplitude sweep from 0.1% shear strain to 1000% shear strain, and the point of gel–sol transition (where G' falls below G'') was recorded (Figure 3C ii). As expected, the coassembled sample performed relatively poorly, undergoing a gel–sol transition at 1.15% shear strain. This relatively poor resistance to shear-strain is likely due to a lack of covalent bonds in this system. In comparison, the LM-GelMA sample demonstrated significantly greater resistance to shear strain, with a gel–sol transition occurring around 450% shear-strain. Interesting, the FPG-hybrid system demonstrated the greatest resistance to shear strain, as indicated by a gel–sol transition at approximately 605% shear-strain. The enhanced ability to resist shear strain in the FPG-hybrid system indicates the hydrogel is acting as a composite system wherein the nanofibrils aid in resisting shear forces when placed in the environment of the well-ordered LM-GelMA network. These enhanced rheological characteristics in the FPG-Hybrid sample are consistent with similar gelatin-nanocomposite systems, wherein the addition

of carbon nanotubes results in substantially enhanced hydrogel rheological properties, including gel–sol transition (fluidized stress), crosslinked stiffness and yield stress.^[34] This is likely due to the integration between the two components, allowing for an increased number density of bonding between the GelMA chains combined with an increase in physical stability due to interactions between GelMA chains and Fmoc-SAP nanofibers, as is seen in similar, gelatin-based systems.^[34] These results support understandings gained through SAXS analysis of mesh size, where a reduced mesh size in the FPG-Hybrid sample is attributed to an increased number density of crosslinks between GelMA macromers comparative to the LM-GelMA sample.

2.4. Investigation of Bioink Printability

Sample printability was investigated to determine the potential of formulated gels as bioink candidates. Initially, a temperature sweep was performed to determine temperatures that may provide suitable printability properties. Here, printability is determined by the ability to deposit a pattern in a controlled manner and the ability of the printed construct to undergo permanent crosslinking to maintain the desired shape. Printability was further assessed through the material's ability to undergo accurate printing across a range of temperatures and the measure of loss tangent ($\tan(\delta)$) was recorded for comparison with existing literature, discussed later. Importantly, relatively low-pressure printing conditions (<69 kPa) were maintained here, which is beneficial for cellular viability.^[35] The thermal dependence of material viscoelastic properties was assessed, and printability studies were undertaken via printing of a dual-layer grid of length 1 cm, strut spacing 2.5 mm with a 22 G needle size (Figure 4A).

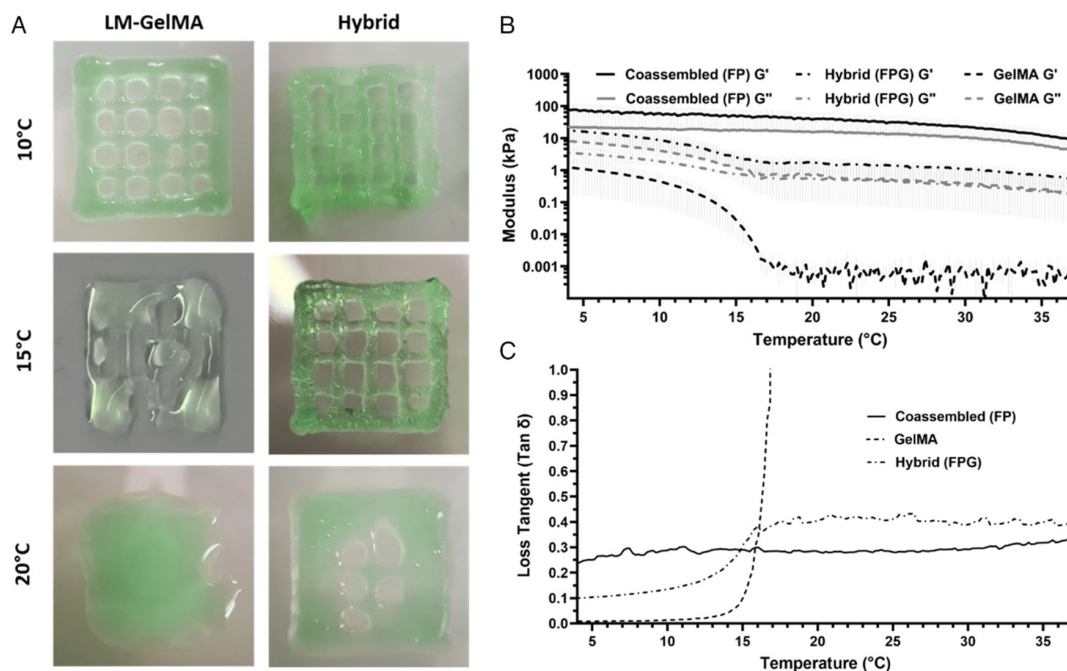


Figure 4. A) Images of material printability through printing of grid (1 cm in length) at 10, 15 and 20 °C. B) Thermoelastic properties of pre-crosslinked materials acquired through oscillatory rheology G' storage modulus (black lines) G'' loss modulus (dark grey lines). C) Loss tangent as a function of temperature. Rheological data is presented as the mean of triplicate tests, light grey lines indicate \pm STD.

2.4.1. Viscoelastic Properties—Rheological Temperature Sweep

Oscillatory rheology was used to investigate material thermo-dependent viscoelastic properties (Figure 4B and S4, Supporting Information). A temperature ramp was selected starting at 37 and cooling to 4 °C. Storage (G') and loss moduli (G'') were monitored for each material, and loss tangent ($\tan \delta$) (G''/G') was recorded (Figure 4B,C). Despite some increases in stiffness upon cooling, the loss tangent of the coassembled system remained constant at approximately 0.3. The coassembled sample demonstrated the stiffest storage moduli of ≈ 87 kPa approaching 4 °C. Contrastingly, LM-GelMA exhibited a significant decrease in loss tangent upon cooling, from >1 to approximately 0.01, with a steep transition evident near 17 °C. LM-GelMA also exhibited the lowest storage modulus ranging from <1 Pa to approximately 2 kPa upon cooling to 4 °C, with no observable change evident between 37 and 18 °C. Interestingly, the FPG-hybrid was found to be a compromise between LM-GelMA and the coassembled sample alone. A thermal dependence was evident, with a notable sudden increase in material stiffness at ≈ 17 °C. FPG-hybrid material storage modulus was found to increase from 650 Pa (37 °C) to 24 kPa (4 °C) following cooling. Interestingly, loss tangent was found to remain relatively constant (0.4) up until approximately 17 °C, after which it decreased to 0.1 at 4 °C. Recently, a study by Gao and colleagues found loss tangent to be a critical factor influencing material extrudability, extrusion uniformity, and structural integrity; ultimately finding loss tangent a suitable measure for indicating material printability in their hybrid alginate-gelatin material.^[36] In their landmark study, the authors report a loss tangent between 0.25 and 0.45 provides an optimal printing window, allowing for suitable extrusion while maintaining good uniformity and structural integrity.^[36] The FPG-hybrid material was found to exist within this range over a substantially large temperature range, from 37.0 to 14.6 °C. Contrastingly, LM-GelMA only existed in this window very briefly from 16.2 to 16.0 °C, during which the gradient was steep and as a result, variance in printability with temperature was significant. Therefore, we anticipated the FPG-hybrid material would exhibit improved printability compared to LM-GelMA over a wider temperature range and would print best near 15 °C.

2.4.2. Optimizing Printed Shape Fidelity via Temperature Control

Following characterization of material thermo-responsive viscoelastic properties, printability was confirmed through printing of grid-like structures. The bioinks were printed at 10, 15, and 20 °C (Figure 4A). Following printing, the coassembled material was unable to maintain shape fidelity under any of the tested conditions and therefore was excluded from all subsequent tests (Figure S5, Supporting Information). Alternatively, LM-GelMA demonstrated relatively good prints at 10 °C following which shape-fidelity reduced as temperature increased (Figure 4A). The FPG-hybrid material was found to produce the best prints out of all the materials, with optimal printing occurring at 15 °C, as expected (printing pressure 42 kPa) (Figure 4A). The FPG-hybrid bioink maintained printability at 10 °C, however

prints were found to be less uniform and required greater pressure (printing pressure 66 kPa), while at 20 °C the FPG-hybrid was observed to be ineffective at maintaining printed geometry (Figure 4A). These results echo previous findings using similar gelatin inspired blends.^[36] Hydrogels were found to remain stable past 4 weeks of simulated culture (PBS, 37 °C) (Figure S6, Supporting Information).

2.5. Investigation of Cytocompatibility

Cytocompatibility of the developed bioink and associated bioprinting process was determined through bioprinting of primary myoblast-containing bioinks under predetermined optimal conditions (10 °C, printing pressure ≈ 30 kPa for LM-GelMA. 15 °C, printing pressure ≈ 40 kPa for FPG-Hybrid). Grid-like structures were printed onto cooled plates and immediately crosslinked under UV light. Directly after printing, cell-laden grids demonstrate structural fidelity and homogenous cellular distribution (Figure S7, Supporting Information). A 2D control was also prepared through seeding of primary myoblasts onto tissue culture plastic.

2.5.1. Viability

Following 24 and 72 h culture, samples were stained with calcein AM (green) and ethidium homodimer (red) to determine the proportion of live and dead cells, respectively. Cells were imaged using fluorescence microscopy (Figure 5 and S7, Supporting Information), and the number of live and dead cells were determined through ImageJ analysis. Following 24 h, the 2D control demonstrated the greatest viability (97.3%) while printed GelMA and FPG-hybrid samples demonstrated lower viabilities of 86.7% and 85.9%, respectively (Figure 5). However, following 72 h culture, all samples demonstrated comparable viabilities ($>98\%$ viability for all samples), indicating that although the printing process resulted in an initial decrease of cell viability, both bioinks supported cell proliferation (Figure 5). These results demonstrate the cytocompatible nature of both materials and the printing process for myoblast bioprinting applications.

2.5.2. Differentiation

The printed constructs were maintained under differentiation conditions for a further 14 days (total 17 days culture). At 7 and 14 days, samples underwent fixation and immunostaining for cell nuclei and cell cytoskeleton and were imaged with confocal to investigate the 3D outcomes. After 7 days under differentiation conditions, the myoblasts had aligned around the printed structures and fused, forming multinucleate bundles at high density with comparable bundle widths (Figure 6 and S8, Supporting Information). The 2D control also exhibited the formation of myotubes; however, the bundle width was significantly smaller (Figure 6). After 14 days differentiation the cells had predominately migrated to the surface of the bioinks (Figure S8, Supporting Information); however, single myoblasts, evidently unfused, could still be seen inside the printed constructs indicating that although the cells had primarily migrated

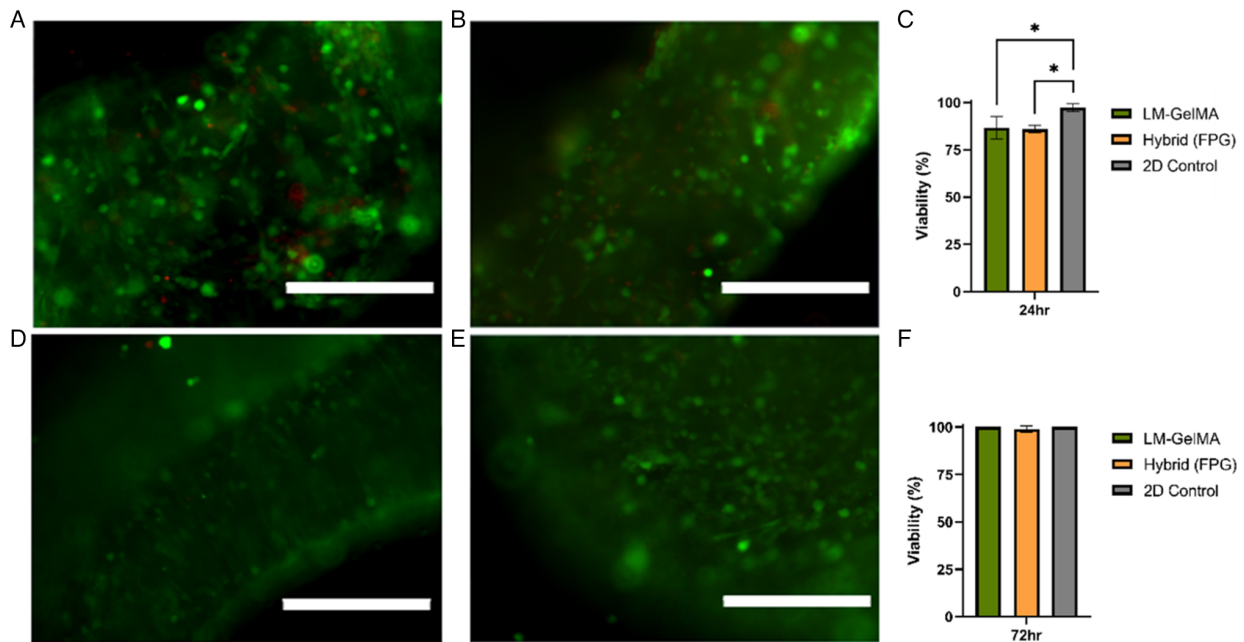


Figure 5. Representative-images of live/dead stain: A) LM-GelMA at 24 h, B) FPG-Hybrid at 24 h, D) LM-GelMA at 72 h, and E) FPG-Hybrid at 72 h (Scale bars 200 μ m). Viabilities of primary skeletal myoblasts on 2D control, or 3D-printed LM-GelMA and FPG-Hybrid at C) 24 h and F) 72 h. Where data represents the mean \pm STD, collected in triplicate ($n = 1$). One way ANOVA was applied to investigate significant differences between groups $* = p < 0.05$.

to the surface, the internal construct was not cytotoxic. At this time point, a slight difference was noted between the bundle width of the developing myotubes on GelMA and the hybrid indicating there may be an effect of material properties on bundle width (Figure 6). Further, the 2D control exhibited significantly smaller bundle widths, indicating an increase in width when culture occurs in these 3D structures. As tissue culture plastic is significantly stiffer than either material, it is unlikely mechanics were the driving factor for changes in bundle width unless a non-linear trend occurs. There was no significant difference in the microstructure of crosslinked GelMA and FPG-Hybrid either. It is then possible that the addition of the diverse bioactive fibers provided a substrate for increased bundle width. GelMA natively contains RGD. In the hybrid sample, additional RGD sites along with PHSRN may have influenced bundle width. Further, the nanofibrous topography may have additionally altered bundle width.

Focused ion beam scanning electron microscopy (FIB-SEM) imaging of the surface further evidenced the formation of myotubes and direct interaction of the cells with the bioink (Figure 7). To image the samples, progressive dehydration with ethanol was undertaken, followed by sputter coating. This progressive dehydration allowed for maintenance of the cell structures and although the dehydrated samples were significantly shrunk in volume the images are representative of the cellular structures and cell-material interaction. FIB-SEM shows evidence of myotube formation and bundling, and provides insight into cell-scaffold interactions. The evidence of multinucleated myotube formation, and high viability affirms the potential for formation of mature muscle tissue using these bioinks.

3. Discussion and Conclusion

Bioink development is a necessary step to rapidly fabricated organs; however, at present, advancement is hindered by the mismatch between recapitulating the complexity of the native ECM and retaining optimal material printability and post-print shape fidelity. Precise control over cell microenvironmental and material properties is key to effective bioink development, the former providing the cues for proliferation, differentiation, and migration, while the latter is the core of spatially deposited viable cells. Both must coexist, and exhibit their vital properties, cells must attach and survive in a controlled manner to develop into a functioning organ suitable for implantation, and the spatial deposition must facilitate integration. The design of specific cell attachment sites through self-assembling peptides, and further development into an effective bioink by merging with LM-GelMA was the focus of this study. Self-assembling peptides Fmoc-FRGDF and Fmoc-PHSRN were coassembled and further combined with LM-GelMA. The coexistence of peptides and macromolecule provides nano- through macro-scale features and proves to be of benefit through the enhancement of bioprintability. Primary myoblast proliferation and differentiation were supported with high cell viability throughout printing and 17-day culture. Thorough material characterization was undertaken demonstrating fibrous morphology (fibril diameter 15 nm), photocuring (8.3 min), shape fidelity, and longevity under culture conditions (4 weeks). This study demonstrates that our developed FPG-hybrid bioink offers improved bioprintability outcomes compared to LM-GelMA and SAPs alone. Further, that the bioink and bioprinting process described here is compatible with primary myoblast differentiation into multinucleated myotubes.

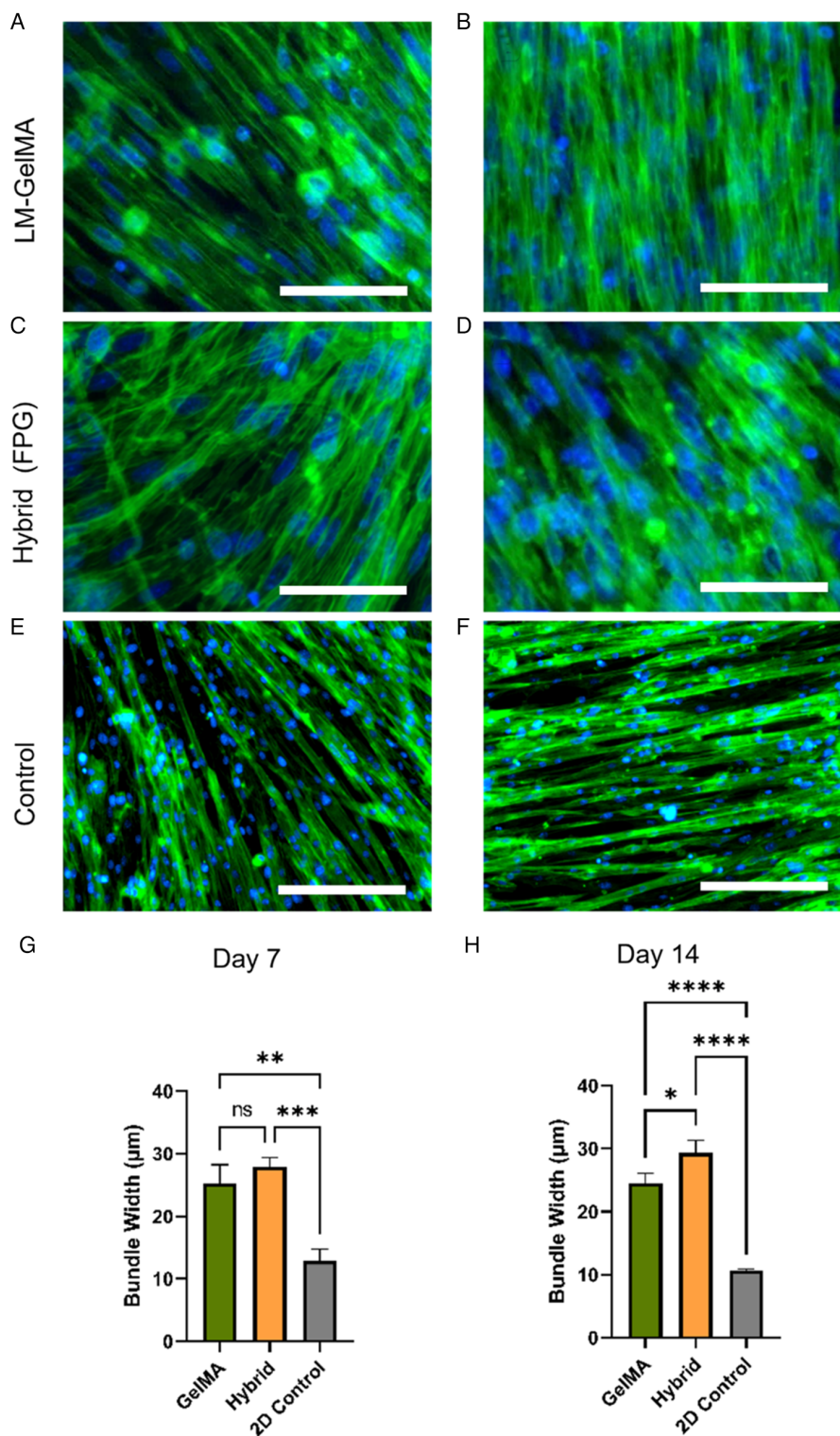


Figure 6. Myoblasts demonstrated the ability to undergo differentiation in A,B) GelMA C,D) Hybrid and E,F) 2D control. G) Evident multinucleated myotubes formed with no significant difference between bundle width in printed samples at day 7 (H). however, by day 14 an increase in bundle width was significant between the GelMA and hybrid. Scale Bars A-F indicate 150 µm. Where data represents the mean ± STD, collected in triplicate ($n = 1$). One way ANOVA was applied to investigate significant differences between groups. Where $* = p < 0.05$, $** = p < 0.01$, $*** = p < 0.001$, and $**** = p < 0.0001$.

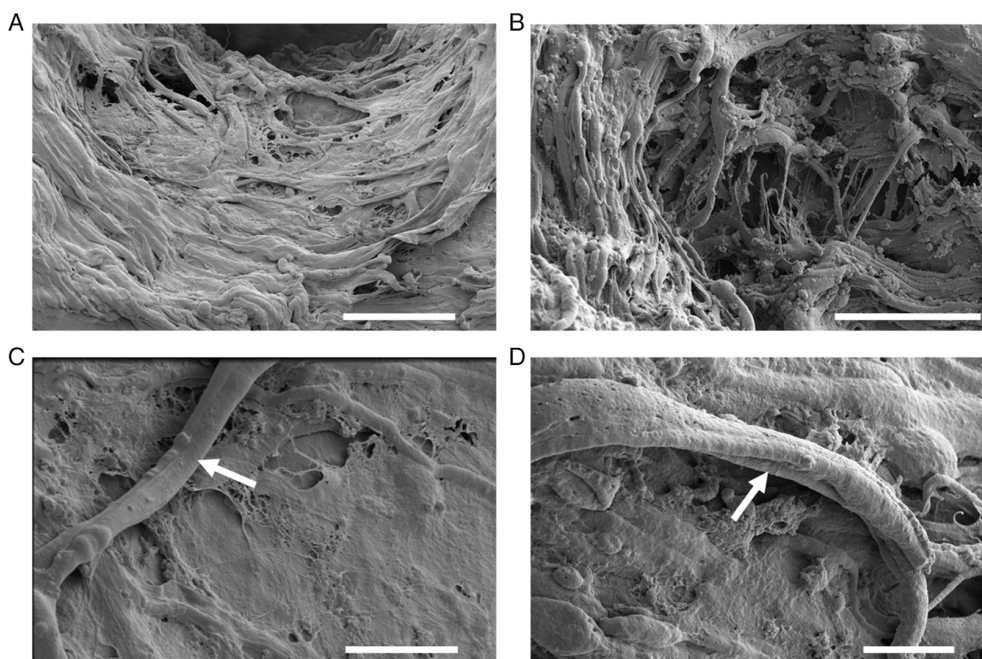


Figure 7. FIB-SEM images after 14 days of differentiation demonstrating myotube formation on A) GelMA bioink, B) hybrid bioink, C) myotube bundle formation on GelMA bioink, and D) myotube bundle formation on hybrid bioink. Arrows showing cell myotube formation. Scale bars: A,B) 50 μm ; C,D) 10 μm .

Our work opens an opportunity for the development of designed, tissue-specific peptide-containing hybrid bioinks. Due to the ease of design of capped peptides, several different cell-attachment motifs may be explored, giving rise to a toolkit of modular peptides to create a tissue-specific bioink with robust printing. Further, the improved temperature stability of the hybrid bioink demonstrated in this study may have application to other thermally sensitive bioinks. Here, the addition of a secondary peptide network was able to provide a benefit of thermal stability so that the necessary properties for extrusion bioprinting were maintained with reduced fluctuation. This concept could be explored, not only for extrusion bioprinting but also other biofabrication methods that rely on consistent material properties for accurate 3D patterning.

Future works should consider self-assembling peptides hybrid materials as bioinks, specifically as peptides can be designed to contain tissue-specific epitopes (here RGD and PHSRN) as well as offering nano-fibrous networks (ECM mimicry) and improved biofabrication outcomes (here, due to temperature stability). Our work demonstrates application to muscle printing; however, our work is limited in that it does not demonstrate full cellular characterization (gene expression) or use a human cell line that would be required for treatment of muscle disorders.^[37] Our future works will build on the knowledge gained here to develop peptide-containing hybrid bioinks as well as a further in-depth characterization of the effects fibrous RGD and PHSRN components on cellular outcomes for improved muscle engineering.

4. Experimental Section

Materials: Fmoc-Self-Assembling-Peptides: TFA-free, desalted Fmoc-FRGDF and Fmoc-PHSRN were purchased from Pepmic (Pepmic Co.,

China) and validated using mass spectrometry. LM-GelMA: LM-GelMA (34% Methacrylate) was obtained from the ANFF Materials Node (University of Wollongong, Australia). All reagents unless otherwise stated were purchased from Sigma-Aldrich.

Bioink Formation: Fmoc-FRGDF/Fmoc-PHSRN coassembled hydrogel was prepared as previously described.^[22] LM-GelMA was prepared by dilution to final concentration of 6% w/v in 1 \times PBS with 0.025% LAP and stored under UV-protected conditions. FPG-hybrid was prepared as Coassembled gel, however before addition of 1 \times PBS, 400 μL of 15% w/v LM-GelMA was added and briefly vortexed such that a final LM-GelMA concentration of 6% w/v was achieved. All samples were held at 37 $^{\circ}\text{C}$ for 72 h prior to use. This method was used to prepare all samples for analysis unless otherwise mentioned.

Cryo-SEM: Samples were prepared as above; however, PBS was replaced with MilliQ (Millipore Co.) to minimize salt bridging and precipitation. Samples were plunged into liquid nitrogen slush (-210°C), immediately transferred to Gatan cryo-chamber attached to the microscope. The samples were fractured inside the cryo chamber and sublimated at -95°C for 2 min to remove amorphous surface ice. Samples were then gold sputter coated for 140 s before being imaged at 15 kV, spot size 5 with FEI Quanta 200 SEM. Samples were maintained at the temperature of -140°C throughout imaging.

TEM

The samples were prepared by negative staining method. Strong carbon-formvar grids (GSCu200C-25) were placed on a 15 μL droplet of sample diluted as 1:5 (Sample: MilliQ water) for 30 s, the excess was blotted with kimwipe. Grids were placed on a 15 μL droplet of uranyl acetate 1% stain for 5 min; excess was blotted with kimwipe and left at room temperature to air dry overnight. All droplets were deposited on parafilm. Bright Field TEM was performed at an accelerating voltage of 80 kV with JEOL 1010 Transmission Electron Microscope. Images were captured by Gatan Orius SC600A camera. TEM fiber dimensions were calculated using ImageJ measurement tool ($n > 5$).

Small-Angle X-Ray Scattering: SAXS was performed at the Australian Synchrotron (Melbourne, Australia) using the SAXS/WAXS beamtime at 5% flux. Measurements were acquired at a calibrated camera length of

967.667 mm with X-ray energy of 12 KeV (1.03320 Å); allowing for scattering vector (q) to be measured across the range of 0.018 to 0.92 Å⁻¹. The diffraction pattern was recorded on a Pilatus 1M detector (169 mm × 179 mm, effective pixel size (172 μm × 172 μm) and processed using the Australian Synchrotron ScatterBrain Software (Melbourne, Victoria, Australia). Hydrogels were prepared as detailed earlier loaded into 1.5 mm sealed glass capillaries with a wall thickness of 0.1 mm (Hilgenberg, GmbH). PBS backgrounds with and without LAP were collected before samples were loaded. Each sample (and background) was subjected to ten 1 s⁻¹ exposures at multiple points along the capillary to minimize sample burning. Repeat measurements were summed using Scatterbrain and q calibrated using an AgBeh sample. The intensity was normalized and set on an absolute scale using water and air shots. Due to poor scattering, backgrounds were scaled by 0.9 before subtraction from the sample scattering data. For coassembled hydrogel fibril radius calculations, data was subject to indirect Fourier transform (IFT) analysis and P(r) inversion using SASView (SASView, Victoria, Australia) to calculate the average diameter of the fibrils in the sample. For LM-GelMA and FPG-Hybrid samples, data were fit to shape independent models using SASView. Specifically, the mass fractal dimension was determined through fitting with power-law model between mid q range (0.05–0.2 Å⁻¹); correlation length was determined through fitting with correlation length model at low-mid q range (0.018–0.2 Å⁻¹); and mesh size was determined through fitting with two power-law model at low-mid q range (0.018–0.2 Å⁻¹). All acquired scatter curves, and subsequent fits were further graphed using GraphPad Prism 7 (GraphPad Prism Software Inc., San Diego, USA) for ease of graphical visualization.

Circular Dichroism: Samples at 50:1 and 500:1 dilution (diluted in MilliQ) were scanned from 330 to 180 nm. Five accumulations were performed for each sample with a 1 nm data interval at 100 nm min⁻¹. A MilliQ background was obtained and subtracted from each sample. Data were smoothed with inbuilt software (Jasco J-815 Circular Dichroism Spectropolarimeter). Data were normalized to molar ellipticity account for relative concentration.

FT-IR: FT-IR spectrums were acquired from a Frontier FT-IR/FIR spectrometer, Bruker D8 XRD (Bruker Co.) from wavelengths 4000–400 cm⁻¹ at a resolution of 1 cm⁻¹. 16 accumulations were performed, and background (1 × PBS) was acquired and subtracted from samples. Data were smoothed with inbuilt software (Frontier FT-IR/FIR spectrometer, Bruker D8 XRD).

Fluorescence Spectroscopy: Fluorescent Spectra were acquired on Perkin Elmer LS 55 Fluorescence Spectrometer using a 10 mm cuvette (Perkin Elmer) from 300 to 600 nm at an excitation wavelength of 250 nm, slit width of 2.5 nm and scan speed of 50 nm min⁻¹.

Rheology: Storage and loss moduli were acquired under oscillatory conditions using a calibrated rheometer (Anton Paar MCR 301, Austria) fitted with a 15-mm cone plate fixture with a cone angle of 1° (CP15-1, Anton Paar GmbH); A thin layer of paraffin oil was placed across the gap to avoid dehydration. Thermal dependent viscoelastic properties were acquired via temperature sweep from 37 to 4 °C at a shear strain of 0.1% and angular frequency of 10 rad s⁻¹. Loss tangent curves were data smoothed using a rolling average ($n=3$) to remove noise. In situ UV crosslinking was performed at a wavelength of 365 nm and intensity of 4.5 mW cm⁻² for 20 min (OmniCure Lx400+, Lumen Dynamics Group Inc.). UV intensity was verified using an OmniCure LED Light Meter System (Lumen Dynamics Group Inc.). Samples were allowed to stabilize for 1 min before UV application. Constant shear strain of 0.1%, the angular frequency of 10 rad s⁻¹ and a temperature of 37 °C were used during UV crosslinking. Amplitude sweep was obtained after full crosslinking via a shear strain logarithmic ramp from 0.1 to 1000% at an angular frequency of 10 rad s⁻¹ and at 37 °C.

Printability Tests: Bioinks were prepared as aforementioned, and immediately placed into 3 mL Optimum syringe barrels (Nordson EFD) after which bioinks were sealed and allowed to self-assemble over 72 h in 37 °C incubation. For temperature printability tests, bioinks were cooled to 10, 15, and 20 °C using an ES SERIES laboratory refrigerator (Thermo Fisher Scientific Australia). Cartridge temperatures were monitored using a FLIRone thermal camera (FLIR Systems Inc.). After cooling, cartridges were fitted with conical 22 G (TT) Blue Precision Tips (Nordson EFD) and

placed into an Inkredible Bioprinter where they were prepared for bioprinting as per manufacturer's recommendations. Briefly, axes were homed, and z-position calibrated. Pneumatic pressure was facilitated through MC mini compressor (MC90, BILTEMA) and further regulated using an AD300C automatic dispenser pressure regulator (Iwashita Instruments). Bioinks were extruded in a grid-like pattern (Figure S5B, Supporting Information) as commanded by in-house developed G-code. Extrusion pressure was adjusted accordingly with changes in viscosity between bioinks and printing temperatures. Pressures ranged between 30 and 60 kPa. Printed grid constructs were printed onto cooled (≈ -20 °C) petri dishes (Greiner Bio-one) and crosslinked immediately after printing at 365 nm and 4.5 mW cm⁻² for 8 min (UVP crosslinker, Analytik Jena). Images were taken both before and after crosslinking. Following crosslinking, samples were fully submerged in 1 × PBS and shape-fidelity (swelling and degradation) was monitored for 4 weeks under simulated culture conditions (PBS, 37 °C).

Myoblast Preparation and Culture: Primary myoblasts were isolated from the hind limb muscles of 5- to 6-week-old C57Bl/6 mice, as previously described, according to ethics protocol 86/06 (St Vincent's Hospital Melbourne, AEC) in accordance with the Australian code of practice for the care of animals for scientific purposes (NHMRC). Myoblasts were maintained under standard tissue culture conditions in growth media consisting of Hams F10 (Gibco), 20% FBS (Gibco), 2.5 ng mL⁻¹ basic FGF (Peprotec), 2 mM L-glutamine (Gibco) and 100 U mL⁻¹ of penicillin (Gibco), and 100 mg mL⁻¹ streptomycin (Gibco) and passaged at 70–80% confluency using standard procedures.

BioPrinting: Bioinks were prepared as above; however, measures to ensure sterility were observed. Specifically, all reagents were prepared sterile. After 72 h formation, the gels were seeded with primary myoblasts (15 million cells mL⁻¹) by brief and gentle vortex. The gel was transferred to the previously sterilized bioink cartridge via 1 mL pipette and cooled to an optimal temperature as determined in printability tests (10 and 15 °C for LM-GelMA and FPG-Hybrid, respectively). Temperature monitored via FLIRone thermal camera to ensure accuracy. Bioinks were printed into a grid as above, and immediately UV crosslinked for 8 min. Bioprinted grids were covered in 2 mL growth media (as described above) and maintained at 37 °C with 1 mL growth media change every 48 h. Triplicate grids were fabricated and analyzed per time point.

Viability Study: At 24 and 72 h in culture 1 mL media was gently removed, Ethium bromide and Calcein AM stains were added and left at 37 °C for 15 min. Stained cells were observed under a fluorescent microscope. Live/Dead cells count was performed using ImageJ cell counter.

Differentiation Study: After 72 h in culture, growth media was aspirated and replaced with differentiation media (DMEM with 2% horse serum, 1% penicillin-streptomycin, 1 × L-glutamine, Lonza). Cells were cultured in differentiation media for up to 14 days with a half media change every 2 days. Triplicate grids were fabricated and analyzed per time point. At 7 and 14 days, media was removed, and cells were fixed with 4% paraformaldehyde in PBS (ProSciTech Pty. Ltd.) overnight. Paraformaldehyde was then removed, and constructs washed twice with PBS followed by a 1 h PBS soak. Cells were solubilized in 0.1% Triton × (ProSciTech Pty. Ltd.) for an hour and washed twice with PBS followed by a 1 h PBS soak. PBS was then removed, and phalloidin (Life Technologies, Australia) was added as per manufactures instructions. Phalloidin was left overnight to ensure good stain penetration through the depth of the print. Again, constructs were washed twice with PBS before a subsequent 1 h PBS soak. PBS was then removed and DAPI (Life Technologies, Australia) was added as per manufactures recommendation. DAPI was stained for 1 h to ensure good stain penetration through the depth of the scaffold. Finally, constructs were washed twice followed by two 1 h PBS soaks. Constructs were then imaged via confocal analysis (Nikon A1R Confocal laser microscope with N-STORM) and morphology assessed as an indication of myogenic differentiation.

Fib-Sem: Primary myoblast interaction with printed bioinks was assessed via SEM following 14 days differentiation. Briefly, cells were fixed in formalin overnight followed by washing thrice in PBS. Samples were then washed three times in 0.1 M cacodylate buffer to avoid salt precipitation. Next, 1% osmium tetroxide was added to samples and samples were

soaked for 30 min. Osmium tetroxide was then removed, and samples were washed three times with MilliQ water. Samples then underwent various drying steps through sequential increase in ethanol content. Specifically, samples were immersed in 50% ethanol for 10 min, followed by soaking in 70% ethanol for 10 min. Samples were then soaked in 90% ethanol for 30 min followed by further soak in 100% ethanol for 30 min. 100% ethanol was then removed, and samples were placed in fresh 100% ethanol overnight at 4 °C. Finally, samples were removed from ethanol and placed onto SEM stubs where they were allowed to dry for a minimum of 1 h. Samples were then gold sputter coated and stored in a sealed environment prior to imaging. Samples were imaged using a FEI Scios Dualbeam FIBSEM and/or FEI Verios 460L FEGSEM.

Statistics: Data in Figure 3–5, and 6 represents mean ± STD of triplicate repeats ($n = 1$). Statistical analysis in Figure 5 and 6 were subject to a one-way ANOVA with Tukey post-hoc test to identify statistically significant differences between groups (GraphPad Prism v9.1.2) where $* = p < 0.05$, $** = p < 0.01$, $*** = p < 0.001$, and $**** = p < 0.0001$.

Supporting Information

Supporting Information is available from the Wiley Online Library or from the author.

Acknowledgements

M.B.-M. and K.F. contributed equally to this work. This research was undertaken on the Small/wide angle X-ray scattering beamline at the Australian Synchrotron, part of ANSTO (Application AS182/SAXS/13541). Viscoelastic properties were performed in the BioFab3D laboratories at St. Vincent's Hospital, Melbourne, Australia. One of the authors (M.B.-M.) was supported by an RMIT Post-Submission Publication Support Grant. One of the authors (K.F.) was supported by an RMIT Engineering Scholarship and an Australian Government Research Training Program Scholarship. One of the authors (A.R.) was supported by an Alfred Deakin Postdoctoral Research Fellowship. One of the authors (D.R.N.) was supported by a NHMRC Dementia Research Leadership Fellowship (GNT1135687). The authors acknowledge the facilities, and the scientific and technical assistance, of the RMIT Microscopy & Microanalysis Research Facility at RMIT University. The authors acknowledge the use of facilities within the RMIT Micro Nano Research Facility (MNRF). The authors thank RMIT staff for their assistance: Assoc. Prof. Paul Ramsland for circular dichroism, Dr. Zeyad Nasa for confocal, and Dr. Cathal O'Connell for rheology.

Conflict of Interest

The authors declare no conflict of interest.

Data Availability Statement

Research data are not shared.

Keywords

bioink, biomaterials, bioprinting, gelatin methacrylate, self-assembling peptides

Received: August 19, 2021

Revised: October 26, 2021

Published online: December 1, 2021

- [1] S.A. Murphy, V. A. Atala, *Nat. Biotechnol.* **2014**, *32*, 773.
- [2] C. L. Hedegaard, E. C. Collin, C. Redondo-Gómez, L. T. Nguyen, K. W. Ng, A. A. Castrejón-Pita, J. R. Castrejón-Pita, A. Mata, *Adv. Funct. Mater.* **2018**, *28*, 1703716.
- [3] M. Kesti, C. Eberhardt, G. Pagliccia, D. Kenkel, D. Grande, A. Boss, M. Zenobi-Wong, *Adv. Funct. Mater.* **2015**, *25*, 7406.
- [4] P. G. Campbell, E. D. Miller, G. W. Fisher, L. M. Walker, L. E. Weiss, *Biomaterials* **2005**, *26*, 6762.
- [5] M. Boyd-Moss, K. Fox, M. Brandt, D. Nisbet, R. Williams, in *Peptides And Peptide-Based Biomaterials And Their Biomedical Applications*, Springer, New York **2017**, pp. 95–129.
- [6] B. J. Klotz, D. Gawlitta, A. J. Rosenberg, J. Malda, F. P. Melchels, *Trends Biotechnol.* **2016**, *34*, 394.
- [7] K. Yue, G. Trujillo-de Santiago, M. M. Alvarez, A. Tamayol, N. Annabi, A. Khademhosseini, *Biomaterials* **2015**, *73*, 254.
- [8] W. Liu, M. A. Heinrich, Y. Zhou, A. Akpek, N. Hu, X. Liu, X. Guan, Z. Zhong, X. Jin, A. Khademhosseini, *Adv. Healthcare Mater.* **2017**, *6*, 1601451.
- [9] W. Xiao, J. Li, X. Qu, L. Wang, Y. Tan, K. Li, H. Li, X. Yue, B. Li, X. Liao, *Mater. Sci. Eng., C* **2019**, *99*, 57.
- [10] A. A. Aldana, L. Malatto, M. A. U. Rehman, A. R. Boccaccini, G. A. Abraham, *Nanomaterials* **2019**, *9*, 120.
- [11] M. Boyd-Moss, K. Firipis, C. O'Connell, A. Rifai, A. F. Quigley, G. Boer, B. Long, D. R. Nisbet, R. J. Williams, *Mater. Chem. Front.* **2021**.
- [12] L. Li, J. Eyckmans, C. S. Chen, *Nat. Mater.* **2017**, *16*, 1164.
- [13] Y. Shao, J. Fu, *Adv. Mater.* **2014**, *26*, 1494.
- [14] J. W. Nichol, S. T. Koshy, H. Bae, C. M. Hwang, S. Yamanlar, A. Khademhosseini, *Biomaterials* **2010**, *31*, 5536.
- [15] C. C. Horgan, A. L. Rodriguez, R. Li, K. F. Bruggeman, N. Stupka, J. K. Raynes, L. Day, J. W. White, R. J. Williams, D. R. Nisbet, *Acta Biomater.* **2016**, *38*, 11.
- [16] R. Li, A. Rodriguez, D. R. Nisbet, C. J. Barrow, R. J. Williams, in *Micro And Nanofabrication Using Self-Assembled Biological Nanostructures*, Elsevier, Amsterdam **2015**, pp. 33–61.
- [17] V. N. Modepalli, A. L. Rodriguez, R. Li, S. Pavuluri, K. R. Nicholas, C. J. Barrow, D. R. Nisbet, R. J. Williams, *Pept. Sci.* **2014**, *102*, 197.
- [18] A. Rodriguez, T.-Y. Wang, K. Bruggeman, C. Horgan, R. Li, R. J. Williams, C. L. Parish, D. Nisbet, *J. Mater. Chem. B* **2014**, *2*, 7771.
- [19] A. Rodriguez, K. Bruggeman, Y. Wang, T.-Y. Wang, R. J. Williams, C. L. Parish, D. Nisbet, *J. Tissue Eng. Regen. Med.* **2018**, *12*, 1571.
- [20] K. Firipis, D. R. Nisbet, S. J. Franks, R. M.E. Kapsa, E. I. Pirogova, R. J. Williams, A. Quigley, *Polymers* **2021**, *13*, 2590.
- [21] R. Li, C. C. Horgan, B. Long, A. L. Rodriguez, L. Mather, C. J. Barrow, D. R. Nisbet, R. J. Williams, *RSC Adv.* **2015**, *5*, 301.
- [22] S.-S. Aye, R. Li, M. Boyd-Moss, B. Long, S. Pavuluri, K. Bruggeman, Y. Wang, C. R. Barrow, D. R. Nisbet, R. J. Williams, *Polymers* **2018**, *10*, 690.
- [23] K. Firipis, M. Boyd-Moss, B. Long, C. Dekiwadia, W. Hoskin, E. Pirogova, D. R. Nisbet, R. M. Kapsa, A. F. Quigley, R. J. Williams, *ACS Biomater. Sci. Eng.* **2021**, *7*, 3340.
- [24] R. Li, M. Boyd-Moss, B. Long, A. Martel, A. Parnell, A. J. Dennison, C. J. Barrow, D. R. Nisbet, R. J. Williams, *Sci. Rep.* **2017**, *7*, 1.
- [25] R. Li, S. Pavuluri, K. Bruggeman, B. M. Long, A. J. Parnell, A. Martel, S. R. Parnell, F. M. Pfeffer, A. J. Dennison, K. R. Nicholas, *Nanomed. Nanotechnol. Biol. Med.* **2016**, *12*, 1397.
- [26] R. Li, N. L. McRae, D. R. McCulloch, M. Boyd-Moss, C. J. Barrow, D. R. Nisbet, N. Stupka, R. J. Williams, *Biomacromolecules* **2018**, *19*, 825.
- [27] A. M. Smith, R. J. Williams, C. Tang, P. Coppo, R. F. Collins, M. L. Turner, A. Saiani, R. V. Ulijn, *Adv. Mater.* **2008**, *20*, 37.
- [28] R. Aston, K. Sewell, T. Klein, G. Lawrie, L. Grøndahl, *Eur. Polym. J.* **2016**, *82*, 1.

- [29] P. W. Schmidt, *J. Appl. Crystallography* **1991**, *24*, 414.
- [30] B. Hammouda, in *Probing Nanoscale Structures-The Sans Toolbox*, National Institute of Standards and Technology, USA **2008**, pp. 1–717.
- [31] E.P. Wisotzki, I. P. Tempesti, E. Fratini, S. G. Mayr, *Phys. Chem. Chem. Phys.* **2017**, *19*, 12064.
- [32] R. A. Hule, R. P. Nagarkar, A. Altunbas, H. R. Ramay, M. C. Branco, J. P. Schneider, D. J. Pochan, *Faraday Discuss.* **2008**, *139*, 251.
- [33] B. Lindemann, U. P. Schröder, W. Oppermann, *Macromolecules* **1997**, *30*, 4073.
- [34] M. Jeong, H. Jang, H.-J. Cha, B. Park, J. Kim, J.-K. Yoo, T. Park, J. W. Yi, D. G. Seong, Y. Oh, *Carbon* **2021**, *184*, 811.
- [35] K. Nair, M. Gandhi, S. Khalil, K. C. Yan, M. Marcolongo, K. Barbee, W. Sun, *Biotechnol. J. Healthc. Nutr. Technol.* **2009**, *4*, 1168.
- [36] T. Gao, G. J. Gillispie, J. S. Copus, A. K. Pr, Y.-J. Seol, A. Atala, J. J. Yoo, S. J. Lee, *Biofabrication* **2018**, *10*, 034106.
- [37] C. Blake, O. Massey, M. Boyd-Moss, K. Firipis, A. Rifai, S. Franks, A. Quigley, R. Kapsa, D. R. Nisbet, R. J. Williams, *APL Bioeng.* **2021**, *5*, 031502.